



Controllable construction of flower-like FeS/Fe₂O₃ composite for lithium storage

Jie Wang^{a,b}, Huan He^a, Zexing Wu^{a,f}, Jianing Liang^a, Lili Han^{c,d}, Huolin L. Xin^{c,e}, Xuyun Guo^b, Ye Zhu^b, Deli Wang^{a,*}

^a Key Laboratory of Material Chemistry for Energy Conversion and Storage (Huazhong University of Science and Technology), Ministry of Education, Hubei Key Laboratory of Material Chemistry and Service Failure, School of Chemistry and Chemical Engineering, Huazhong University of Science and Technology, China

^b Department of Applied Physics, The Hong Kong Polytechnic University, Hung Hom, Kowloon, Hong Kong

^c Center for Functional Nanomaterials, Brookhaven National Laboratory, Upton, NY 11973, USA

^d Center for Electron Microscopy, TUT-FEI Joint Laboratory, Institute for New Energy Materials & Low-Carbon Technologies, School of Materials Science and Engineering, Tianjin University of Technology, Tianjin 300384, China

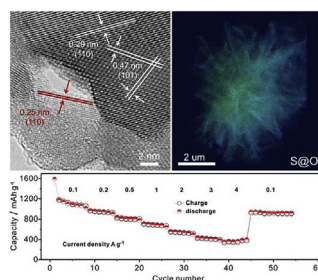
^e Department of Materials Science and Engineering, Stony Brook University, Stony Brook, NY, 11794, USA

^f Key Laboratory of Sensor Analysis of Tumor Marker of Education Ministry; State Key Laboratory Base of Eco-chemical Engineering, College of Chemistry and Molecular Engineering Qingdao University of Science & Technology 53 Zhengzhou Road, 266042, Qingdao, China

HIGHLIGHTS

- Controllable construction of flower-like FeS/Fe₂O₃ composite.
- Such composite features porous structure with surface Fe₂O₃ coverage.
- The synergistic effect between FeS and Fe₂O₃ shows excellent battery performance.

GRAPHICAL ABSTRACT



ARTICLE INFO

Keywords:

Flower-like FeS/Fe₂O₃ composite
Porous structure
Synergistic performance
Lithium storage
Volume discharging/charging compatibility

ABSTRACT

Transitions metal sulfides/oxides have been considered as promising anode candidates for next generation lithium-ion batteries (LIBs) due to high theoretical capacities. However, the large volume change during lithiation/delithiation process and poor electronic conductivity often result in a poor charging/discharging performance. Herein, we design a flower-like FeS/Fe₂O₃ composite via a simple “solvothermal-oxidation” method, in which the Fe₂O₃ is most distributed on the surface of the flower. The unique porous structure and synergistic effect between FeS and Fe₂O₃ not only accommodate the large volume expansion, but also facilitate Li ion and electron transport. The Fe₂O₃ shell effectively reduce the dissolution of Li₂S_x during discharge/charge process. When serving as the anode material in lithium ion battery, FeS/Fe₂O₃ exhibits superior specific capacity, rate capacity and cycling stability compared with pure FeS and Fe₂O₃.

1. Introduction

Transition metal sulfides/oxides have been considered as one of

potential alternative lithium ion batteries (LIBs) anode materials for conventional graphite because of their high theoretical capacity, low cost and environmental friendly merits [1–7]. However, the low

* Corresponding author.

E-mail address: wangdl81125@hust.edu.cn (D. Wang).

intrinsic conductivity of metal sulfides/oxides leading to significant irreversible capacity losses and cycling stability. Moreover, the pulverization of metal sulfides/oxides and subsequent detachment from the current collectors induced by large volume changes during charging/discharging processes, which also hinder their commercial application. Among various types of metal sulfides/oxides served as anode materials, iron-based sulfides (FeS) and oxides (Fe_2O_3 or Fe_3O_4) have received particular attention [7–12], since they are expected to have high capacity and outstanding cycling performance [13–16]. However, it still remains challenging for these new anode materials to be large-scale applications. The Li storage process in the conversion reaction of FeS involves generations of Li_2S_x , which is easy to dissolve in a liquid electrolyte, leading to capacity degradation and deteriorate the conductivities of the battery system [17–19]. When Fe_2O_3 was used as anode materials, the large volume change and poor conductivity of the electrode materials during lithiation/delithiation process would lead to the disappointing electrochemical performance [20–22]. Great efforts have been made on controlling the morphology of these materials, such as hollow spheres [23,24], nanorods [25], microboxes [26,27] et al. However, the current synthetic method for morphology controlling of materials are usually either complicated or uneconomical.

In this paper, we report a facile strategy for the preparation of flower-like $\text{FeS}/\text{Fe}_2\text{O}_3$ nanocomposite with porous structure. The unique structure not only enlarges the surface area and shortens the continuous path of Li ion diffusion, but also provides enough space to accommodate the volume change during the discharge/charge process. Meanwhile, the Fe_2O_3 shell could effectively reduce the dissolution of Li_2S_x into the electrolyte and FeS improves the electronic conductivities. Owing to the unique structure and the synergistic effect between FeS and Fe_2O_3 , the $\text{FeS}/\text{Fe}_2\text{O}_3$ composite served as anode for lithium battery exhibits excellent electrochemical performance with a high reversible capacity of 906.7 mAh g^{-1} at a current density of 0.1 A g^{-1} after 100 cycles, which is much higher than pure FeS and Fe_2O_3 electrodes.

2. Experimental part

2.1. Materials synthesis

The synthesis of FeS was based on the simple solvothermal method. In a typical synthesis, 4 mmol of $\text{FeCl}_2 \cdot 4\text{H}_2\text{O}$ and 8 mmol thiourea were dissolved in ethylene glycol, then the solution was transferred into 50 mL of Teflon autoclave and maintained at 200°C for 24 h under autogenous pressure. After cooled down to room temperature, the product was collected by centrifugation and washed with absolute ethanol three times. The flower-like FeS nanoparticles were obtained after 12 h drying under vacuum oven at 60°C .

The flower-like nanoparticles were placed into the tube furnace again and heated to 450°C and 550°C with a heating rate of 1°C min^{-1}

in air atmosphere for 10 h and then the flower-like $\text{FeS}/\text{Fe}_2\text{O}_3$ composite with porous structure and pure Fe_2O_3 were obtained after cooling down to room temperature.

2.2. Material characterization

X'Pert PRO diffractometer, and diffraction patterns were collected using $\text{Cu K}\alpha$ ($\lambda = 1.5406 \text{ \AA}$) radiation at a scanning rate of 4° min^{-1} . Thermal gravimetric analysis (TGA) was carried out on TA-Q500 Instrument with a heating rate of $10^\circ\text{C min}^{-1}$. X-ray photoelectron spectroscopy (XPS) was conducted by using an AXIS-ULTRA DLD-600 W Instrument. The morphologies were examined by scanning electron microscopy (SEM, Sirion200). S/TEM images were obtained using aberration-corrected Hitachi HD2700C and JEOL JEM-2100F equipments operated at 200 keV. Raman spectra were taken by a LabRam HR800 spectrometer with a 532 nm laser excitation. The nitrogen sorption isotherms measurements were conducted by using TriStar II 3020.

2.3. Electrochemical measurements

Electrochemical measurements were carried out by using CR 2032 coin cells assembled in an argon-filled glove box with lithium metal as the anode. The working electrode are comprised of electrode material, carbon black (super-p) and polymer binder (polyvinylidene fluoride: PVDF) in a weight ratio of 70:20:10, using a Cu-foil as the current collector. The two electrodes were separated by a polymeric material (Celgard 2320) and electrolyte was 1.0 M LiPF_6 in a 1:1 ratio of EC (Ethylene carbonate): DEC (Diethylene carbonate). The galvanostatic charge/discharge measurements were tested in the voltage window from 0.05 to 3.0 V using NEWARE battery tester at room temperature. Cyclic voltammetry (CV) testing of the cells was performed on a CHI 1040C (CH Instrument) electrochemistry working station at a scan rate of 0.1 mV s^{-1} . Electrochemical impedance spectroscopy (EIS) was measured on the coin cell using an Autolab PG302N electrochemical workstation. The amplitude of the AC signal applied to the electrode is 10 mV and the frequency range from 100 kHz to 0.1 Hz.

3. Results and discussion

The flower-like $\text{FeS}/\text{Fe}_2\text{O}_3$ composite with porous structure was synthesized through a facile and efficient solvothermal reaction followed by controlled oxidation in air (see details in the [supporting information](#)). As can be seen from the X-ray diffraction (XRD) patterns in Fig. 1a, the solvothermal product was characterized as FeS where diffraction peaks appeared at 29.91° , 33.95° , 44.10° and 53.38° , which can be indexed to the (110), (112), (114) and (300) planes of troilite FeS (JCPDS NO. 37-0477). Since there is no predominant peak in the XRD pattern, indicating that there is no preferred orientation during the

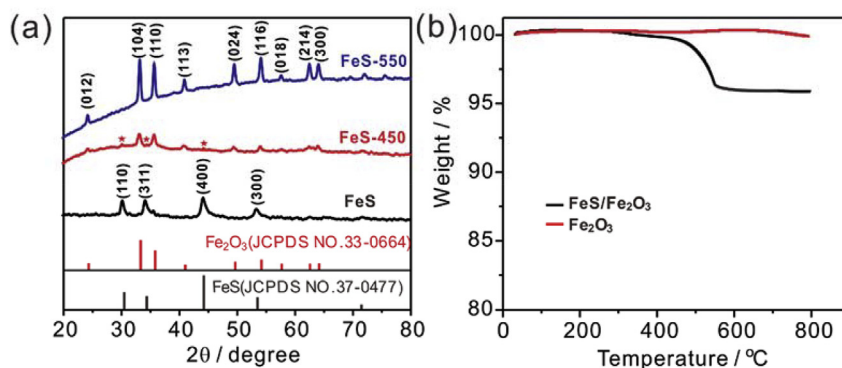


Fig. 1. (a) XRD patterns of FeS before and after oxidized in air at 450°C and 550°C ; (b) TGA curve for the $\text{FeS}/\text{Fe}_2\text{O}_3$ composite and Fe_2O_3 tested in flowing air at a heating rate of $10^\circ\text{C min}^{-1}$.

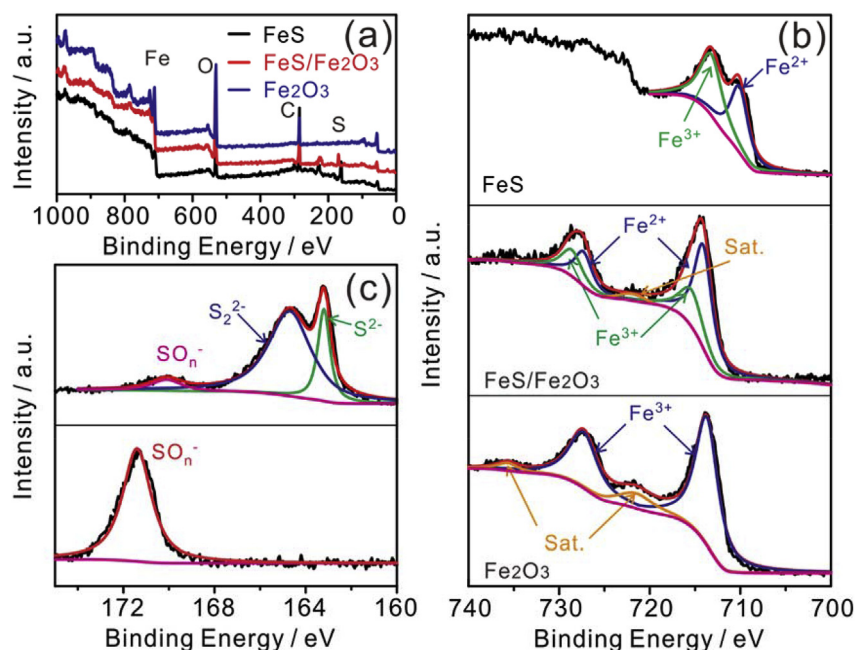


Fig. 2. (a) Full-range XPS spectrum of FeS, FeS/Fe₂O₃ composite and Fe₂O₃; (b) Corresponding high-resolution XPS spectrum of Fe 2p; (c) High resolution XPS spectrum of S 2p in FeS and FeS/Fe₂O₃ composite.

growth of FeS. After oxidized in air at 450 °C, most of the diffraction peaks could be matched to the phase of Fe₂O₃ (JCPDS NO. 33-0664). The peaks at 33.2°, 35.7°, 49.7°, 54.2° and 64.2° agree well with the (104), (110), (024), (116) and (300) planes of Fe₂O₃, respectively, while small peaks (asterisk marks) represent the remained FeS [28]. The intensity of all diffraction peaks of Fe₂O₃ increased with elevating the oxidation temperature (550 °C), suggesting the increased crystallinity and particle size of Fe₂O₃. Moreover, the weight percentage of the remained FeS in FeS/Fe₂O₃ was further tested via thermo-gravimetric analysis in flowing air (Fig. 1b). It can be seen that Fe₂O₃ shows no obvious weight loss even up to 800 °C, suggesting a complete oxidation of Fe₂O₃, while FeS/Fe₂O₃ composite exhibited a weight loss of nearly 4%, indicating a weight percentage of 44.0% for FeS in FeS/Fe₂O₃ composite.

The surface chemical compositions information and the valence states of the FeS, FeS/Fe₂O₃ composite and Fe₂O₃ were analyzed via x-ray photoelectron spectroscopy (XPS). As can be seen from the full-range XPS spectrum in Fig. 2a, five characteristic peaks located at ca. 165, 228, 285, 533 and 725 eV are corresponding to S 2p, S 2s, C 1s, O 1s, and Fe 2p, respectively. With increasing the oxidation temperature, the intensity of the S peaks decreased obviously and disappeared at 550 °C, indicating that the fully oxidation of FeS [29]. The fact that the relative intensity of S for FeS/Fe₂O₃ composite is lower than FeS may due to the surface coverage of Fe₂O₃. On the contrary, the intensity of O peak increased remarkably. The corresponding high-resolution XPS spectrum for Fe 2p are shown in Fig. 2b. As for FeS, the characteristic peaks of Fe 2p_{3/2} are deconvoluted into two characteristic peaks, corresponding to Fe³⁺ and Fe²⁺ valent [30], revealing that the surface of FeS slightly oxidized when exposed in air. After oxidized in air at 450 °C, the characteristic peaks changed significantly, where binding energies at around 713.5 and 725.4 eV, are corresponding to the Fe₂O₃ phase of Fe 2p_{3/2} and Fe 2p_{1/2} [31], indicating a higher oxidation degree of FeS. As the temperature continue to rise, the surface state of the sample has no significant change at higher oxidation temperature. Besides, compared with FeS and Fe₂O₃ samples, the location of characteristic peaks of FeS/Fe₂O₃ composite was fall in between, indicating the interaction of FeS and Fe₂O₃ for FeS/Fe₂O₃ composite which would influence the lithium storage performance. Fig. 2c shows the spectrum of S 2p, the fitting line peaks of FeS sample at 163.1, 164.5 eV and

170.1 eV are corresponding to S²⁻, S_n²⁻ and some oxidation of the surface [32], respectively. In comparison, only oxidized S was detected for FeS/Fe₂O₃ composite, also indicated the oxidation states of the sample. According to the XPS analysis, it is concluded that FeS/Fe₂O₃ composite possess the physical features of FeS and Fe₂O₃, which may exhibit the properties of both of them for lithium storage.

The morphology and microstructure of the samples were characterized using scanning electron microscopic (SEM) and high angle annular dark field scanning transmission electron microscopy (HAADF-STEM), which are shown in Fig. 3. It is obvious that the solvothermal product of FeS exhibited a flower-like structure with micro-size diameter (Fig. 3a) which showed uniform distribution. By enlarging the magnification for one of a particle (Fig. 3b), thin layer can be seen obviously which can denoted as the petal of the flower. After oxidized at 450 °C, FeS/Fe₂O₃ composite still remained the flower-like morphology (Fig. 3c, d and Fig. S1), while the morphology pure Fe₂O₃ oxidized at 500 °C was considerably altered with some of the petals destroyed (Fig. 3e, f and Fig. S2). The slightly enlarged TEM and HAADF-STEM images of FeS/Fe₂O₃ composite (Fig. S3) proved the existence of porous structure, and the pore diameter were most ranging from ca. 5 nm to ca. 50 nm. In order to investigate the surface area information of the three electrode materials, the nitrogen sorption isotherms measurements were conducted which can be seen in Fig. S4. As a result, the specific surface area is calculated to be 12.2 m² g⁻¹, 59.1 m² g⁻¹ and 55.9 m² g⁻¹ for FeS, FeS/Fe₂O₃ composite and Fe₂O₃ materials, respectively. It is clearly showed that the surface area increased after a moderate oxidation of 450 °C, while higher oxidation temperature result in a slightly decrease of surface area. Besides, the adsorption isotherm of FeS/Fe₂O₃ composite exhibits an obvious hysteresis loop, indicating a mesoporous structure which is consistent to the TEM results in Fig. S3. The existence of porous structure and enlarged surface area would not only provide enough channels for the interaction between electrolyte and active materials, and then shorten the reaction distance, but also effectively accommodate the volume change during the discharging/charging process. As for Fe₂O₃, a steep rise close to the high pressure (P/P₀ = 1) was showed which may ascribed to the formation of macroporous structure at higher oxidation temperature [33,34]. The increase of pore size may result in the collapse of the particle and then reduced battery performance. The

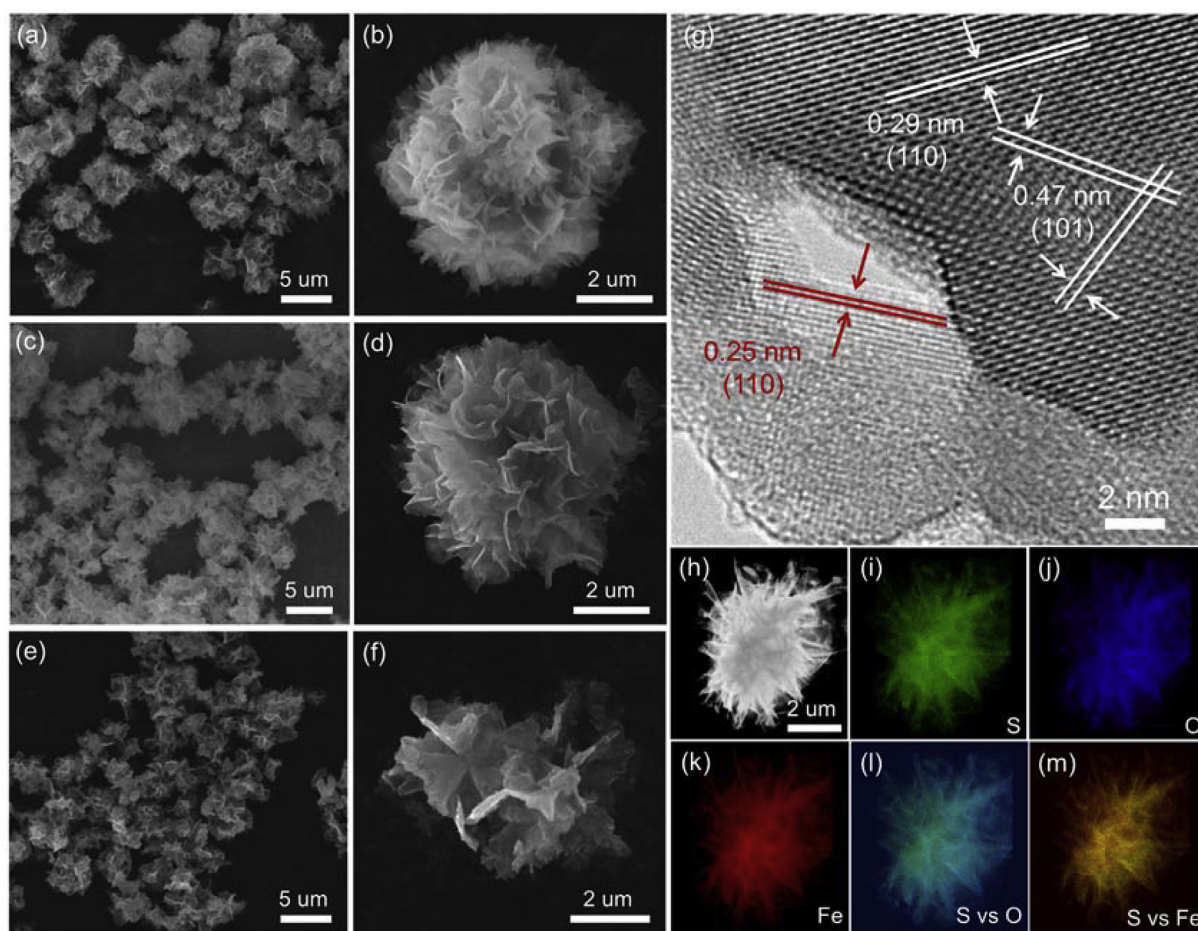


Fig. 3. Overview and single particle SEM images of the flower-like FeS (a, b), FeS/Fe₂O₃ composite (c, d) and Fe₂O₃ (e, f); (g) HRTEM image of the flower-like FeS/Fe₂O₃ composite, (h) HAADF-STEM image of a FeS/Fe₂O₃ particle (h) and the corresponding EDS element mapping of S (i), O (j), Fe (k), overlay of S and O (l) as well as the overlay of S and Fe (m).

formation of the porous structure can be explained via the “Kirkendall” effect [35–37] due to the different migration rate of S and O at air atmosphere with temperature up to 450 °C. It can be seen from the high-resolution TEM image (HRTEM) in Fig. 3g that the inter-planar spacing between adjacent fringes (red lines) is measured to be 0.25 nm, corresponding to the (110) plane of Fe₂O₃, while the other two groups of adjacent fringes (white lines) have the spacings of 0.47 nm and 0.29 nm, corresponding to the (101) and (110) plane of FeS, respectively, consistent with the surface Fe₂O₃ coverage structure of the composite. To further illustrate the specific distribution of FeS and Fe₂O₃, X-ray energy dispersive spectroscopy (EDS) elemental distribution of the FeS/Fe₂O₃ composite was obtained. It can be seen from the HAADF-STEM image and the corresponding elemental mappings in Fig. 3h–m that Fe, O and S elements are distributed uniformly inside the particle. It should be noted that the particle showed O rich at the surface, further suggesting an enrichment of Fe₂O₃ on the surface of the nanostructure, consistent with the coverage structure of FeS/Fe₂O₃ composite. In order to confirm the oxidation reaction was taken place on the surface of the particle, enlarged EDS mapping on part of a petal for FeS/Fe₂O₃ composite was conducted, which can be seen in Fig. S5. The distribution of S was mainly in the thick area and covered by O which confirmed that FeS was covered by Fe₂O₃ on the surface. The existence of Fe₂O₃ on the surface could effectively reduce the dissolution of Li₂S_x into the electrolyte during the discharge/charge process. In comparison, the elemental distribution of Fe₂O₃ was also characterized via EELS mapping (Fig. S6) which proved that there was almost no FeS after the high-temperature oxidation, indicating the complete oxidation

of FeS.

The electrochemical performance of the FeS, FeS/Fe₂O₃ composite and Fe₂O₃ were investigated in a CR2032 coin cell. Fig. 4a shows the cyclic voltammogram (CV) curves of FeS/Fe₂O₃ electrode at a scan rate of 0.1 mV s^{−1}. In the first cycle, the reduction peak at 0.75 V corresponds to Li insertion into Fe₂O₃ and the formation of Fe and Li₂O. In addition, another two reduction peaks were found at around 1.15 V and 1.75 V compared with the CV curves by using Fe₂O₃ as anode (Fig. S7b). The additional small peaks are attributable to the presence of FeS in the electrode, which is consistent with the CV curves by using FeS as anode (Fig. S7a). In detail, the small peak at around 1.75 V corresponds to the transformation of FeS to Li₂FeS₂ and the peak at 1.15 V results from the conversion reaction of FeS + 2Li⁺ + 2e[−] = Li₂S + Fe [38]. The broad anodic peaks at around 1.5 V and 2.0 V are likely ascribed to the oxidation reactions of Fe to Fe₂O₃ and Li₂-xFeS₂ [13], respectively. Different from FeS, Fe₂O₃ electrodes and previous reports, the intensity and position of the main reduction peak at 0.75 V slightly changed in the second cycle, indicating a highly reversible lithiation/delithiation reactions for the FeS/Fe₂O₃ electrode material [9,23,39–41]. Fig. 4b displays the discharge/charge voltage profiles of FeS/Fe₂O₃ electrode for the first five cycles at a current density of 0.1 A g^{−1}. In the first discharge curve, the plateaus located at around 1.7 V and 0.9 V were attributed to the lithiation of FeS and Fe₂O₃, respectively. Compared with the first discharge/charge curves of FeS and Fe₂O₃ (Fig. S8), the discharge plateau of FeS/Fe₂O₃ electrode showed distinct voltage plateau which agreed well with the CV curve. The initial discharge capacity and Coulombic efficiency of FeS/Fe₂O₃ electrode is 1552.9 mAh

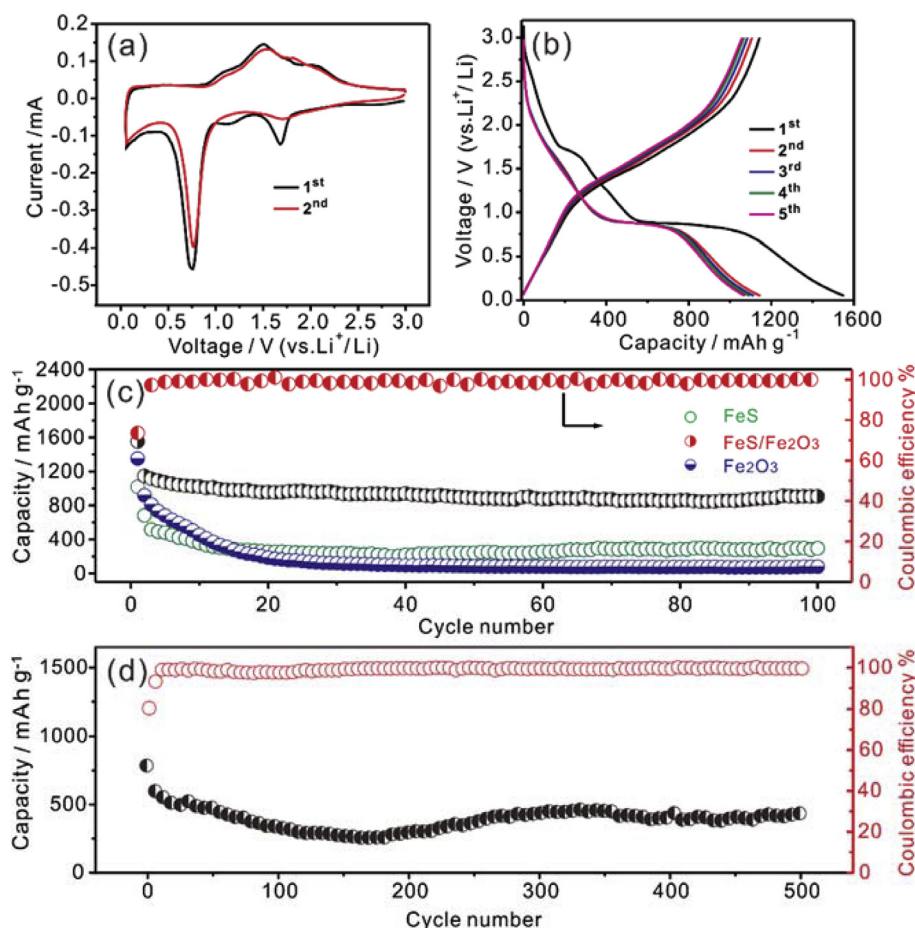


Fig. 4. (a) CV curves of the FeS/Fe₂O₃ electrode for the first two cycles at a scan rate of 0.1 mV s⁻¹; (b) discharge/charge profiles of the FeS/Fe₂O₃ electrode at a current density of 0.1 A g⁻¹; (c) cycling performance of FeS, FeS/Fe₂O₃ composite and Fe₂O₃ electrodes as well as corresponding coulombic efficiency for FeS/Fe₂O₃ electrode at a current density of 0.1 A g⁻¹; (d) long-term cycling performance of FeS/Fe₂O₃ composite at a current density of 2 A g⁻¹.

g⁻¹ and 74%, respectively, which is much higher than FeS (1020 mAh g⁻¹, and 70%) and Fe₂O₃ (1351.5 mAh g⁻¹, 66%). Especially, the relative lower capacity of Fe₂O₃ (with higher theoretical capacity) than FeS/Fe₂O₃ composite may ascribed by the decreasing utility of active materials due to the insulation property of Fe₂O₃. In addition, FeS/Fe₂O₃ composite showed a stable discharge/charge stability in the subsequent four cycles, while FeS and Fe₂O₃ suffer from obvious capacity loss due to the lack of shell protection (Figs. S7c–d). It should be noted that the larger practical capacity than the theoretical capacity could be attributed the irreversible reactions, such as decomposition of electrolytes and the solid electrolyte interface (SEI) formation on the surface of the electrode materials [42]. In terms of the measurement above, FeS/Fe₂O₃ composite electrode exhibits high initial discharge/charge capacities and Coulombic efficiency, due to the unique structure and synergistic effect.

The cycling performances of the electrode materials are shown in Fig. 4c at a current density of 0.1 A g⁻¹ for 100 cycles. Among the three electrodes, FeS/Fe₂O₃ composite shows slightly decayed in the initial 15 cycles and stabilized in the subsequent cycles. In comparison, FeS and Fe₂O₃ electrodes exhibit poor cycling stability and relative low capacities. After 100 cycles, the reversible capacity of FeS/Fe₂O₃ electrode still retained 906.7 mAh g⁻¹, whereas FeS and Fe₂O₃ electrodes were only 295 and 79.1 mAh g⁻¹, respectively. In addition, the coulombic efficiency of FeS/Fe₂O₃ electrode rapidly increases from about 74% for the first cycle and stabilized at around 98.5% after two cycles, indicating fast ion and electron transport in the composite electrodes. When the current density was increased to 0.2 A g⁻¹, the discharge capacity (Fig. S9) slightly decrease in the initial 50 cycles, but gradually back to 1164 mAh g⁻¹ after 200 cycles, which was a common phenomenon for transition metal oxides anode materials [43,44]. For better understanding the FeS/Fe₂O₃ cell in higher cycling rate, the long-

term stability at a current density of 2 A g⁻¹ was investigated which can be seen in Fig. 4d. The FeS/Fe₂O₃ cell showed excellent first discharge capacity of 790 mAh g⁻¹ and retained at ca. 500 mAh g⁻¹ after several cycles with near 100% coulombic efficiency. The capacity remained at 460 mAh g⁻¹ after 500 cycles, indicating excellent cycling stability at high rate.

To further verify the excellent rate performance of the LiBs, Fig. 5a shows the discharge/charge rate performance of FeS/Fe₂O₃ electrode at current densities ranging from 0.1 to 4 A g⁻¹. It can be clearly seen that the FeS/Fe₂O₃ electrode with unique structure exhibits excellent rate performance, and, satisfactory, the discharge capacity maintained at 710 mAh g⁻¹ when the current density was 1 A g⁻¹. The specific capacity attain 390 mAh g⁻¹, when the current density was enhanced to 4 A g⁻¹, which is still higher than the theoretical capacity of graphite. Furthermore, when the current density was restored to 0.1 A g⁻¹, the capacity recovered to 930 mAh g⁻¹, which is very close to the initial capacity. The excellent rate performance of the FeS/Fe₂O₃ electrode is believed to originate from the synergistic effect of FeS and Fe₂O₃ as well as the unique flower-like porous structure.

Electrochemical impedance spectroscopy (EIS) was used to explore the insight electrode kinetics for the excellent electrochemical performance of FeS/Fe₂O₃ composite. Fig. 5b shows the Nyquist plots of two fresh coin cells using FeS, FeS/Fe₂O₃ composite and Fe₂O₃ as electrode materials. It can be seen clearly that the three cells share a common feature with a depressed semicircle in high frequency (R_{ct}) and a linear tail in low frequency region. The equivalent circuit model and the corresponding fitted impedance parameters are shown in Fig. S10 and Table S1. The diameter of the semicircle for FeS/Fe₂O₃ (R_{ct} = 57.4 Ω) fresh cell is between FeS (R_{ct} = 44.2 Ω) and Fe₂O₃ (R_{ct} = 86.8 Ω), indicating that the more the oxidation extent, the higher the resistance [45]. After 15 cycles, the diameter of the semicircle for the FeS/Fe₂O₃

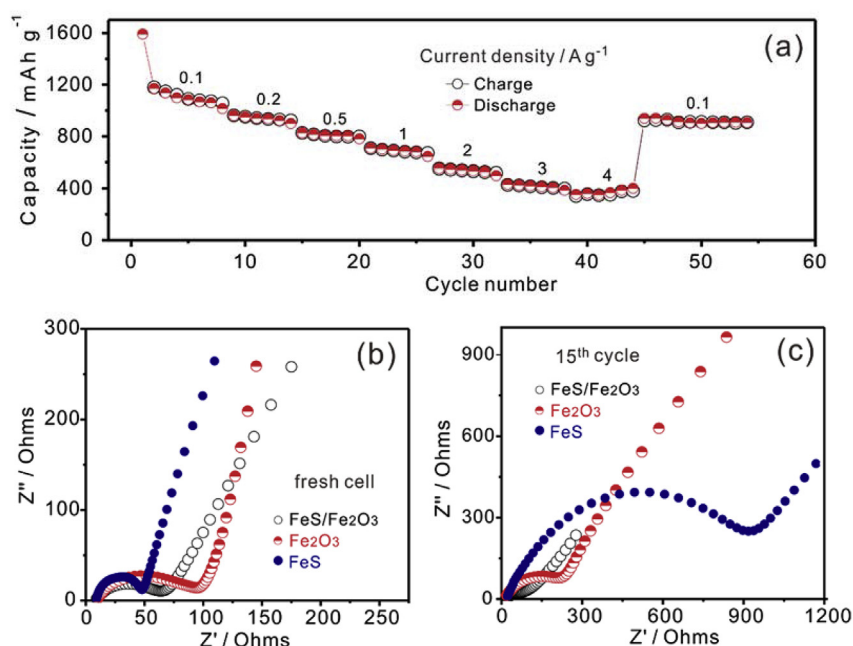


Fig. 5. (a) Rate performance of FeS/Fe₂O₃ composite at current densities from 0.1 A g⁻¹ to 4 A g⁻¹. Nyquist plots of FeS/Fe₂O₃ composite and Fe₂O₃ electrode materials before (b) and after 15 cycles (c).

($R_{ct} = 28.9 \Omega$) decreased compared with the fresh cell, indicating an obvious improvement of charge transfer rate after cycles. In comparison, the charge transfer resistance of FeS ($R_{ct} = 1121.5 \Omega$) and Fe₂O₃ ($R_{ct} = 241.8 \Omega$) increased after cycles (Fig. 5c). The increasing resistance of FeS would be ascribed to its poor rechargeable stability with solid structure, meanwhile, the increasing resistance of Fe₂O₃ may due to the structural collapse after full oxidation. Thus, it can be concluded that the unique flower-like FeS/Fe₂O₃ electrode with porous structure could effectively accelerate electron conductivity and shorten migration distances of lithium ion, which favored cycling stability and high-rate capability.

To further verify the excellent electrochemical performance of FeS/Fe₂O₃ composite, TEM image and corresponding EELS element mapping of S, O and Fe was conducted for a cell after 100 cycles at a current density of 0.1 A g⁻¹. As can be seen from Fig. S11 that the porous structure remained well after cycling performance. In addition, homogeneously distribution of the composite as well as enrichment of O on the outside (compared with S element) proved the coverage structure furtherly which demonstrated the excellent structural stability of FeS/Fe₂O₃ composite.

4. Conclusions

In summary, we have proposed a facile and efficient solvothermal strategy for the synthesis of FeS nanoparticles and followed by post-heated in air atmosphere to obtain flower-like FeS/Fe₂O₃ composite with porous structure. As anode material for LIBs, the composite exhibited high reversible capacity, good rate performance and excellent cycling stability. The synergistic effect of FeS and Fe₂O₃ with unique structure effectively increased the electronic conductivity of FeS/Fe₂O₃ composite. Moreover, the porous structure could accommodate the volume change and shorten the migration distances of lithium ion during the charge/discharge process.

Acknowledgements

This work was supported by the National Natural Science Foundation (21573083), 1000 Young Talent (to Deli Wang). The authors thank the Analytical and Testing Center of HUST for XRD, STEM

measurements. This research used resources of the Center for Functional Nanomaterials, which is a U.S. DOE Office of Science Facility, at Brookhaven National Laboratory under Contract No. DE-SC0012704, and Department of applied physics, The Hong Kong Polytechnic University, which are supported by the Hong Kong Research Grants Council through the Early Career Scheme (Project No. 25301617) and the Hong Kong Polytechnic University grant (Project No. 1-ZE6G). J.W. and Y.Z. thanks Dr. Lu Wei for optimizing the JEOL JEM-2100F microscope.

Appendix A. Supplementary data

Supplementary data related to this article can be found at <http://dx.doi.org/10.1016/j.jpowsour.2018.04.107>.

References

- [1] X. Zhu, Y. Zhu, S. Murali, M.D. Stoller, R.S. Ruoff, Nanostructured reduced graphene oxide/Fe₂O₃ composite as a high-performance anode material for lithium ion batteries, *ACS Nano* 5 (2011) 3333–3338.
- [2] X. Jia, Y. Cheng, Y. Lu, F. Wei, Building robust carbon nanotube-interweaved-nanocrystal architecture for high-performance anode materials, *ACS Nano* 8 (2014) 9265–9273.
- [3] G. Zhang, X.W.D. Lou, General synthesis of multi-shelled mixed metal oxide hollow spheres with superior lithium storage properties, *Angew. Chem.* 126 (2014) 9187–9190.
- [4] J. Wang, N. Yang, H. Tang, Z. Dong, Q. Jin, M. Yang, D. Kisailus, H. Zhao, Z. Tang, D. Wang, Accurate control of multishelled Co₃O₄ hollow microspheres as high-performance anode materials in lithium-ion batteries, *Angew. Chem.* 125 (2013) 6545–6548.
- [5] L. Yu, L. Zhang, H.B. Wu, G. Zhang, X.W.D. Lou, Controlled synthesis of hierarchical Co_xMn_{3-x}O₄ array micro-/nanostructures with tunable morphology and composition as integrated electrodes for lithium-ion batteries, *Energy Environ. Sci.* 6 (2013) 2664–2671.
- [6] Q. Wang, L. Jiao, Y. Han, H. Du, W. Peng, Q. Huan, D. Song, Y. Si, Y. Wang, H. Yuan, CoS₂ hollow spheres: fabrication and their application in lithium-ion batteries, *J. Phys. Chem. C* 115 (2011) 8300–8304.
- [7] H. Hwang, H. Kim, J. Cho, MoS₂ nanoplates consisting of disordered graphene-like layers for high rate lithium battery anode materials, *Nano Lett.* 11 (2011) 4826–4830.
- [8] B. Wu, H. Song, J. Zhou, X. Chen, Iron sulfide-embedded carbon microsphere anode material with high-rate performance for lithium-ion batteries, *Chem. Commun.* 47 (2011) 8653–8655.
- [9] B. Wang, J.S. Chen, H.B. Wu, Z. Wang, X.W. Lou, Quasiemulsion-templated formation of α -Fe₂O₃ hollow spheres with enhanced lithium storage properties, *J. Am. Chem. Soc.* 133 (2011) 17146–17148.

- [10] K.-A. Kwon, H.-S. Lim, Y.-K. Sun, K.-D. Suh, α -Fe₂O₃ submicron spheres with hollow and macroporous structures as high-performance anode materials for lithium ion batteries, *J. Phys. Chem. C* 118 (2014) 2897–2907.
- [11] X. Xu, R. Cao, S. Jeong, J. Cho, Spindle-like mesoporous α -Fe₂O₃ anode material prepared from MOF template for high-rate lithium batteries, *Nano Lett.* 12 (2012) 4988–4991.
- [12] M. Reddy, T. Yu, C.-H. Sow, Z.X. Shen, C.T. Lim, G. Subba Rao, B. Chowdari, α -Fe₂O₃ nanoflakes as an anode material for Li-Ion batteries, *Adv. Funct. Mater.* 17 (2007) 2792–2799.
- [13] C. Xu, Y. Zeng, X. Rui, N. Xiao, J. Zhu, W. Zhang, J. Chen, W. Liu, H. Tan, H.H. Hng, Controlled soft-template synthesis of Ultrathin C@FeS nanosheets with high-Li-storage performance, *ACS Nano* 6 (2012) 4713–4721.
- [14] S. Kostov, M. denboer, E. Strauss, D. Golodnitsky, S. Greenbaum, E. Peled, X-ray absorption fine structure studies of FeS₂ cathodes in lithium polymer electrolyte batteries, *J. Power Sources* 81 (1999) 709–714.
- [15] F. Han, D. Li, W.C. Li, C. Lei, Q. Sun, A.H. Lu, Nanoengineered polypyrrole-coated Fe₂O₃/C multifunctional composites with an improved cycle stability as lithium-ion anodes, *Adv. Funct. Mater.* 23 (2013) 1692–1700.
- [16] J.M. Jeong, B.G. Choi, S.C. Lee, K.G. Lee, S.J. Chang, Y.K. Han, Y.B. Lee, H.U. Lee, S. Kwon, G. Lee, Hierarchical hollow spheres of Fe₂O₃@Polyaniline for lithium ion battery anodes, *Adv. Mater.* 25 (2013) 6250–6255.
- [17] C. Wang, H. Chen, W. Dong, J. Ge, W. Lu, X. Wu, L. Guo, L. Chen, Sulfur–amine chemistry-based synthesis of multi-walled carbon nanotube–sulfur composites for high performance Li–S batteries, *Chem. Commun.* 50 (2014) 1202–1204.
- [18] P.G. Bruce, S.A. Freunberger, L.J. Hardwick, J.-M. Tarascon, Li–O₂ and Li–S batteries with high energy storage, *Nat. Mater.* 11 (2012) 19–29.
- [19] Z.-S. Wu, Y. Sun, Y.-Z. Tan, S. Yang, X. Feng, K. Müllen, Three-dimensional graphene-based macro- and mesoporous frameworks for high-performance electrochemical capacitive energy storage, *J. Am. Chem. Soc.* 134 (2012) 19532–19535.
- [20] Q. Su, D. Xie, J. Zhang, G. Du, B. Xu, In situ transmission electron microscopy observation of the conversion mechanism of Fe₂O₃/Graphene anode during lithiation–delithiation processes, *ACS Nano* 7 (2013) 9115–9121.
- [21] S. Xu, C.M. Hessel, H. Ren, R. Yu, Q. Jin, M. Yang, H. Zhao, D. Wang, α -Fe₂O₃ multi-shelled hollow microspheres for lithium ion battery anodes with superior capacity and charge retention, *Energy Environ. Sci.* 7 (2014) 632–637.
- [22] G. Zhou, D.-W. Wang, P.-X. Hou, W. Li, N. Li, C. Liu, F. Li, H.-M. Cheng, A nanosized Fe₂O₃ decorated single-walled carbon nanotube membrane as a high-performance flexible anode for lithium ion batteries, *J. Mater. Chem.* 22 (2012) 17942–17946.
- [23] D. Wang, Y. Yu, H. He, J. Wang, W. Zhou, H.D. Abruña, Template-free synthesis of hollow-structured Co₃O₄ nanoparticles as high-performance anodes for lithium-ion batteries, *ACS Nano* 9 (2015) 1775–1781.
- [24] D. Wang, H. He, L. Han, R. Lin, J. Wang, Z. Wu, H. Liu, H.L. Xin, Three-dimensional hollow-structured binary oxide particles as an advanced anode material for high-rate and long cycle life lithium-ion batteries, *Nanomater. Energy* 20 (2016) 212–220.
- [25] Y.-M. Lin, P.R. Abel, A. Heller, C.B. Mullins, α -Fe₂O₃ nanorods as anode material for lithium ion batteries, *J. Phys. Chem. Lett.* 2 (2011) 2885–2891.
- [26] P. Lou, Y. Tan, P. Lu, Z. Cui, X. Guo, Novel one-step gas-phase reaction synthesis of transition metal sulfide nanoparticles embedded in carbon matrices for reversible lithium storage, *J. Mater. Chem.* 4 (2016) 16849–16855.
- [27] P. Du, L.X. Song, J. Xia, Y. Teng, Z.K. Yang, Construction and application of α -Fe₂O₃ nanocubes dominated by the composite interaction between polyvinyl chloride and potassium ferrocyanide, *J. Mater. Chem.* 2 (2014) 11439–11447.
- [28] Z. Ma, X. Huang, S. Dou, J. Wu, S. Wang, One-pot synthesis of Fe₂O₃ nanoparticles on nitrogen-doped graphene as advanced supercapacitor electrode materials, *J. Phys. Chem.* 118 (2014) 17231–17239.
- [29] M. Descostes, F. Mercier, N. Thomat, C. Beaucaire, M. Gautier-Soyer, Use of XPS in the determination of chemical environment and oxidation state of iron and sulfur samples: constitution of a data basis in binding energies for Fe and S Reference compounds and applications to the evidence of surface species of an oxidized pyrite in a carbonate medium, *Appl. Surf. Sci.* 165 (2000) 288–302.
- [30] X. Wang, Q. Xiang, B. Liu, L. Wang, T. Luo, D. Chen, G. Shen, TiO₂ modified FeS nanostructures with enhanced electrochemical performance for lithium-ion batteries, *Sci. Rep.* 3 (2013) 2007.
- [31] X. Wei, W. Li, J.-a. Shi, L. Gu, Y. Yu, FeS@C on carbon cloth as flexible electrode for both lithium and sodium storage, *ACS Appl. Mater. Interfaces* 7 (2015) 27804–27809.
- [32] E.-J. Kim, J.-H. Kim, A.-M. Azad, Y.-S. Chang, Facile synthesis and characterization of Fe/FeS nanoparticles for environmental applications, *ACS Appl. Mater. Interfaces* 3 (2011) 1457–1462.
- [33] K.S. Sing, Reporting physisorption data for gas/solid systems with special reference to the determination of surface area and porosity, *Pure Appl. Chem.* 57 (1985) 603–619.
- [34] J. Wang, H.L. Xin, J. Zhu, S. Liu, Z. Wu, D. Wang, 3D hollow structured Co₂FeO₄/MWCNT as an efficient non-precious metal electrocatalyst for oxygen reduction reaction, *J. Mater. Chem.* 3 (2015) 1601–1608.
- [35] Y. Yin, R.M. Rioux, C.K. Erdonmez, S. Hughes, G.A. Somorjai, A.P. Alivisatos, formation of hollow nanocrystals through the nanoscale kirkendall effect, *Science* 304 (2004) 711–714.
- [36] L. Han, Q. Meng, D. Wang, Y. Zhu, J. Wang, X. Du, E.A. Stach, H.L. Xin, Interrogation of bimetallic particle oxidation in three dimensions at the nanoscale, *Nat. Commun.* 7 (2016) 13335.
- [37] J. Wang, Z. Wu, L. Han, R. Lin, H.L. Xin, D. Wang, Hollow-Structured carbon-supported nickel cobaltite nanoparticles as an efficient bifunctional electrocatalyst for the oxygen reduction and evolution reactions, *ChemCatChem* 8 (2016) 736–742.
- [38] Y. Xu, W. Li, F. Zhang, X. Zhang, W. Zhang, C.-S. Lee, Y. Tang, In situ incorporation of FeS nanoparticles/carbon nanosheets composite with an interconnected porous structure as a high-performance anode for lithium ion batteries, *J. Mater. Chem.* 4 (2016) 3697–3703.
- [39] C. Xing, D. Zhang, K. Cao, S. Zhao, X. Wang, H. Qin, J. Liu, Y. Jiang, L. Meng, In situ growth of FeS microsheet networks with enhanced electrochemical performance for lithium-ion batteries, *J. Mater. Chem.* 3 (2015) 8742–8749.
- [40] G. Huang, F. Zhang, X. Du, Y. Qin, D. Yin, L. Wang, Metal organic frameworks route to in situ insertion of multiwalled carbon nanotubes in Co₃O₄ polyhedra as anode materials for lithium-ion batteries, *ACS Nano* 9 (2015) 1592–1599.
- [41] J. Wang, H. Zhou, J. Nanda, P.V. Braun, Three-dimensionally mesostructured Fe₂O₃ electrodes with good rate performance and reduced voltage hysteresis, *Chem. Mater.* 27 (2015) 2803–2811.
- [42] D. Gu, W. Li, F. Wang, H. Bongard, B. Spliethoff, W. Schmidt, C. Weidenthaler, Y. Xia, D. Zhao, F. Schüth, Controllable synthesis of mesoporous peapod-like Co₃O₄@Carbon nanotube arrays for high-performance lithium-ion batteries, *Angew. Chem. Int. Ed.* 54 (2015) 7060–7064.
- [43] G. Yang, H. Cui, G. Yang, C. Wang, Self-assembly of Co₃V₂O₈ multilayered nanosheets: controllable synthesis, excellent Li-Storage properties, and investigation of electrochemical mechanism, *ACS Nano* 8 (2014) 4474–4487.
- [44] G. Zhang, L. Yu, H.B. Wu, H.E. Hoster, X.W.D. Lou, formation of ZnMn₂O₄ ball-in-ball hollow microspheres as a high-performance anode for lithium-ion batteries, *Adv. Mater.* 24 (2012) 4609–4613.
- [45] B. Guo, C. Li, Z.-Y. Yuan, Nanostructured Co₃O₄ materials: synthesis, characterization, and electrochemical behaviors as anode reactants in rechargeable lithium ion batteries, *J. Phys. Chem. C* 114 (2010) 12805–12817.